crystals

MDPI

Article

Effect of Prior Surface Textures on the Resulting Roughness and Residual Stress during Bead-Blasting of Electron Beam Melted Ti-6Al-4V

Mustafa Rifat, Saurabh Basu *, Edward C. De Meter and Guha Manogharan

Industrial and Manufacturing Engineering, Pennsylvania State University, University Park, PA 16801, USA; mxr652@psu.edu (M.R.); ecd3@psu.edu (E.C.D.M.); gum53@psu.edu (G.M.)
* Correspondence: sxb514@psu.edu

Abstract: The finishing of additive manufactured (AM) components is crucial for endowing them with fatigue resistance. Unfortunately, current AM processes naturally promote anisotropic surface characteristics that make it challenging to optimize finishing processes. In this study, bead-blasting is explored as a process for finishing Electron Beam Melted (EBM) Ti-6Al-4V. The effects of anisotropic roughness characteristics on the mechanics of bead-blasting are delineated using surface texture measurements via optical profilometry and residual stress measurements via X-ray diffraction. As-received surfaces resulting from AM, as well as those that have been Electrical Discharge Machined (EDM), are studied. It is seen that pre-processed roughness textures heavily influence the final textures and residual stresses. These linkages are quantified using a plasticity index as the governing metric—a rougher surface features a larger plastic index, which results in comparatively greater evolution of its texture characteristics than a smoother surface after equivalent bead-blasting treatments. The mechanics of this evolution are delineated using energy-controlled indentation as a model representing a single impact in bead-blasting. It is seen that rougher surfaces featuring complex textures in as-received states also produce complex stress states featuring a greater level of locally tensile stresses during indentation compared with smoother surfaces. Approaches to address these complications are proposed that can potentially transform a printed, non-functional surface into one that is optimized for fatigue resistance.

Keywords: additive manufacturing; electron beam melting; bead-blasting; surface roughness; residual stress

Citation: Rifat, M.; Basu, S.; De Meter, E.C.; Manogharan, G. Effect of Prior Surface Textures on the Resulting Roughness and Residual Stress during Bead-Blasting of Electron Beam Melted Ti-6Al-4V. *Crystals* **2022**, *12*, 374. https://doi.org/10.3390/cryst12030374

Academic Editors: Samo Kralj, Alexandre A.S. Goncalves, Cristiane Alves Pereira, Liping Zhang and Kele Tatiane Gomes Carvalho

Received: 11 January 2022
Accepted: 2 March 2022
Published: 10 March 2022

1. Introduction

Powder bed, additive manufacturing (AM) processes are a popular means to print metallic, near-net-shape parts. Using these processes, a part is printed in layers. For each printed layer, a high energy beam, typically a laser or electron, traces a pattern on a bed of powder overlaying a previously printed part layer. The beam melts the powder as well as one or more previously solidified layers of the part. The resultant melt pool solidifies to yield the shaped part with a new layer of metal.

The texture of a printed surface varies with surface orientation relative to the build direction. Two factors that principally affect it are stair-casing and partial powder solidification. Stair-casing [1] results from the discrete, layer–layer solidification of a surface. It leaves behind ridges with nearly repetitive peak-to-peak spacing. The peak-to-valley height of the ridges is most pronounced on surfaces that are neither parallel nor perpendicular to the build direction. The peak-to-valley height is typically much smaller on vertical, ruled surfaces that are parallel to the build direction. Stair-casing is typically not observed on top and flat surfaces orthogonal to the build direction. Partial powder solidification [2] results from metal powder lying partially outside of the melt pool. This results in metal globs fusing to the stair-cased surface. It affects all surfaces, except for top, flat surfaces

orthogonal to the build direction. The texture of downward facing surfaces is typically dominated by this effect and exceptionally rough.

A printed surface typically lacks the geometric precision and smoothness required for typical, functional surface requirements. Consequently, hard-tool machining processes, such as machining or grinding, are applied to critical regions to strip away a thin layer (typically less than 1 mm) of metal to generate functional surfaces. Ordinarily, the total area of these functional surfaces is but a small fraction of the total part area. For most applications, this is all the surface modification that is required. However, for high-performance fatigue applications, secondary processes are applied to smooth the non-functional surfaces. These secondary processes are much faster and cheaper to apply than hard tool machining. Surface smoothing maybe achieved either through metal subtraction or metal redistribution. An advantage of the latter is that it is typically accompanied by the development of compressive residual stresses within the surface and surface sublayer. This is desirable since it further enhances fatigue resistance.

A process that is commonly used for metal redistribution is bead-blasting [3,4]. This process involves spraying glass beads onto the treated surface using pressurized air. The impact of individual glass beads with the surface plastically deforms asperities and results in the accumulation of plastic deformation in the sub-surface volume, whereby the creation of compressive residual stresses is realized. The mechanics of bead-blasting have been extensively studied, and the effects of process parameters, such as coverage [5], bead diameter, impact velocity [6], distance, angle [7], duration [8], almen intensity [9], media type [10], and temperature [11], on the resulting surface integrity have been delineated. Recently, novel modifications to this process have also been proposed, e.g., via temporal gradients to accelerating pressure, which is gradually increased during surface treatment. This results in better spatial and temporal control on surface hardening, which eventually results in a longer fatigue life in components [12].

The effects of substrate hardness on the mechanics of bead-blasting are also well investigated. In very hard and brittle materials, such as ceramics, bead-blasting can deteriorate surface quality by generating cracks [13], unless the process is precisely controlled by tuning its parameters [14,15]. Nonetheless, bead-blasting is often performed on hard metallic surfaces. This is because thicker surface hardened layers, e.g., those resulting from case hardening, result in the percolation of plastic strains that originate from bead-blasting to larger depths compared with analogous substrates that are not case-hardened [16]. This percolation produces beneficial compressive residual stresses up to greater depths underneath the surface, which increases fatigue life [17]. The mechanics underlying these phenomena and their microstructural underpinnings have been delineated using finite elements [18–21]. The effect of the currently existing mechanical state quantified as its initial residual stress field (IRSF) has also been studied. Sherafatnia et al. showed that a tensile IRSF on the surface of a thin sample increases the depth of compressive residual stress that result from bead-blasting. Conversely, such an IRSF decreases the depth of the same for thick samples [17]. Similar studies on samples where IRSF was induced by welding were carried out by Hatamleh et al. [22] and Sidhom et al. [23].

An important aspect of the impact treatment processes that likely affect their mechanics and eventual efficacy is the initial surface roughness condition of the substrate. Arifvianto et al. investigated the effect of the starting roughness of the samples on the final roughness attained after surface mechanical attrition treatment (SMAT). They experimentally showed that smoother AISI 316L surfaces become rougher, while rough AISI 316L surfaces become smoother after processing using SMAT. Further, surfaces that were rougher to start with ended with larger saturating R_a values than surfaces that were smooth in their starting condition. They hypothesize from these results that the initial surface roughness can affect the final saturating roughness achievable by bead-blasting. However, initial roughness characteristics do not affect the work hardening during impact treatment [24,25]. The effect of initial surface integrity on bead-blasting was also studied by Xu et al. They pre-processed a large surface area of electron-beam-melted Ti-6Al-4V by: (i) end-milling,

(ii) surface-grinding, (iii) abrasive water-jet-machining, and (iv) wire electric discharge machining. Subsequently, they performed shot-peening on these pre-processed surfaces. They reported that the abrasive jet-machined + shot-peened specimens showed the best fatigue performance. This benefit was attributed to the compound effect of the abrasive water jet action followed by the shot-peening action [26].

Sample surfaces that are shot-peened are usually flat. However, they can have curvatures associated with them, i.e., they can be convex or concave. Ref. [27] delineates the effects of curved surfaces on the mechanics of shot peening. It reports that an increase in surface curvature can be correlated to an increase in the maximum and surface compressive residual stress after shot-peening. Interestingly, the behavior was found to be similar for both convex and concave surfaces.

While significant research has been performed on numerous aspects of impact treatments, the effect or surface roughness textures relevant to additive manufacturing on the mechanics of bead-blasting are not well understood. Currently, research has largely focused on how surface processing routines can be optimized to reduce surface roughness and enhance fatigue life [28,29]. However, how the starting surface texture affects the mechanics of the impact treatment processes and accompanying residual stress development is currently unknown. This research attempts to answer this question for metal parts printed from Ti-6Al-4V powder using the Electron Beam Powder Bed Fusion (EBPBF) process [30,31]. This process, which typically yields greater surface roughness than Laser Powder Bed Fusion, was chosen for this reason [4,32,33]. This paper first describes an experimental study that was used to characterize the effect that the starting texture has on surface topography and residual stress evolution. It then presents a plasticity index model that is combined with surface texture interferometry data to explain the sensitivity of the surface texture's evolution to the starting texture. It then presents a micro-scale deformation model that was used to describe the deformation and residual stress evolution resulting from the impact of a single bead with a surface whose texture is equivalent to that obtained using the EBPBF process.

2. Experimental

Ti-6Al-4V samples were printed using the EBM process on Arcam A2 Electron Beam Melting machine (General Electric, Cincinnati, OH, USA). Arcam specified Ti-6Al-4V powder was used in the process [34]. The size of the powder particles was about 50 µm (D 95%). The surface temperature for processing was 750 °C. The parts were printed with a layer thickness of 70 µm and a beam overlap of 200 µm. Beam diameter and power of the machine were maintained in the range of 0.20–1.00 mm and 50–3500 W, respectively. The effective contour speed, support speed, and melt speed were ∼17.18 mm/s, 50 mm/s, and 500 mm/s, respectively. A total time of 1200 min was provided for the build to cool down to room temperature.

Figure 1 shows the two EBM specimens that were printed for this study. While the aforementioned process parameters were maintained across the two specimens, their geometry was changed to produce one cube featuring a horizontal top surface and another quadrilateral with its top surface aligned at 30° with respect to the horizontal. Following the build, a Hansvedt model DS2 (Hansvedt EDM, Rantoul, IL, USA) wire electric discharge machine (EDM) was used to cut the printed specimens into various sections along the dashed lines shown in Figure 1. One of the objectives of this study was to determine the effect of the as-received surface roughness, which results from additive manufacturing, on the final roughness and residual stress after bead-blasting. Prior studies have reported that inclined surfaces resulting from additive manufacturing have higher roughness compared to the surfaces that are parallel or perpendicular to the build direction [35–38]. Further, these roughness textures have been shown to assume the greatest R_a values when their parent surfaces have inclinations in the range of 5°–45° [36]. This observation leads to the choice of a 30° surface for delineating the mechanics of bead-blasting in our study.

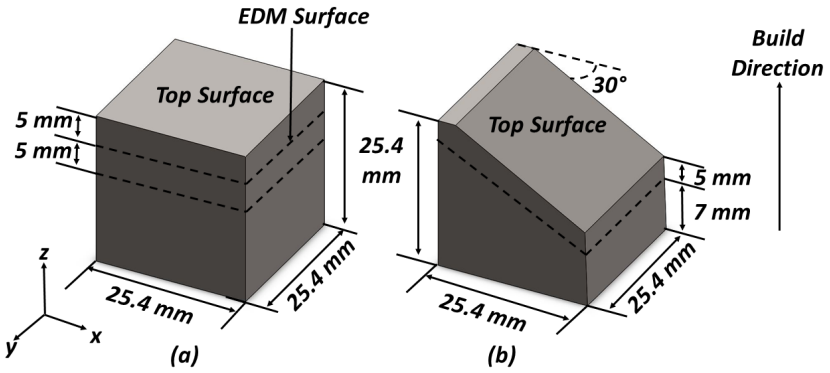

Figure 1. Schematic of the samples: (**a**) Sample 1 and (**b**) Sample 2; the dashed lines show the sections cut from the samples for analysis.

The aforementioned (e.g., as-received and EDM) sections obtained from AM builds were bead-blasted using Potters C(40–60) metal finishing media (Potters Industries LLC, 143 Malvern, PA, USA) that had a nominal diameter (D 50%) of about 369 µm for 300 s. The size distribution of beads was characterized via laser scattering using the Malvern Panalytical Mastersizer 3000 (Malvern Panalytical Inc., Westborough, MA, USA). This duration selected for bead-blasting (300 s) was determined based on references [39–41]. The blasting unit utilized high-pressure air to accelerate the media. Air pressure of 0.41 MPa (∼60 Psi) was used. The blasting nozzle was maintained using a c-clamp at a fixed height ∼216 mm (8.5 inch) and oriented perpendicularly with respect to the surface being treated (see Figure 2 for setup and bead size distribution).

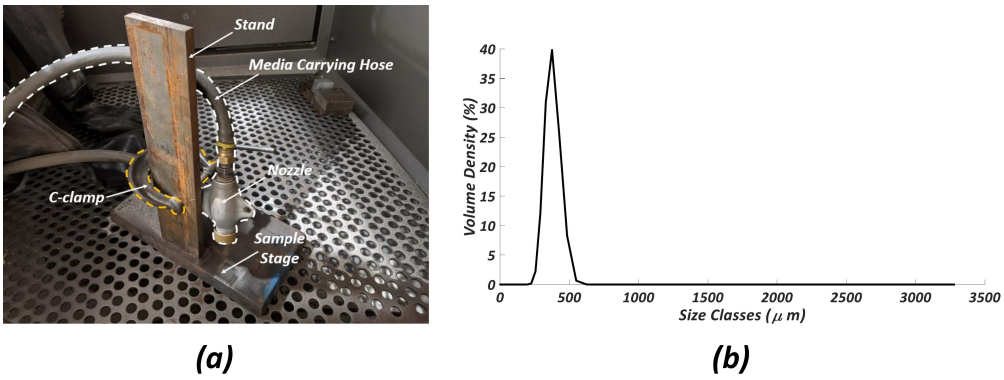

Figure 2. (**a**) The bead-blasting stage with the nozzle clamped on; (**b**) Bead size distribution.

Surface roughness was measured before and after bead-blasting on all cross-sections using a Zygo Nexview optical white light profilometer (Zygo Corporation, Middlefield, 153 CT, USA). A 20× × 2× magnification was used to perform the white light profilometry for sample 1. However, the large roughness in the as-received (top) surface of sample 2 made it more challenging to perform white light profilometry. This challenge was mitigated by using a smaller magnification of 20× × 0.5×. Various surface roughness parameters, e.g., S_a, S_q, and S_z, were extracted from the white light scans.

Residual stress measurements were performed using a Malvern Panalytical X'Pert3 MRD X-ray Diffraction (XRD) machine that was equipped with a 4-circle goniometer (Malvern Panalytical B.V., Almelo, The Netherlands). All sections created were scanned before and after bead-blasting to find residual stress in both states. Residual stresses were measured via the the $\sin^2\psi$ method by characterizing the $(10\bar{1}3)$ peak corresponding to Bragg angle of 70.8° [42,43]. A ±2° window was scanned around this Bragg angle. A Copper radiation source ($\lambda = 1.5604$ Å) was used with a step size of 0.03° and time per step of 40 s. A 1.5 mm divergence slit and axial beam mask were used during the

XRD. Generator tension and current for the experiments were set at 45 KV and 40 mA, respectively. As the sample tilts at different ψ angles, the irradiated area changes during the scan. The maximum area at $\psi = 71.57^{\circ}$ was about 70 mm^2. The X-ray penetration depth is limited to 50 µm [44], so the residual stress derived using this method is representative of that in the surface.

The mechanics of surface deformation during unit impacts in bead-blasting were simulated using the Abaqus numerical finite element package. To this end, energy-controlled indentation was used as a model of unit impact. This involved quasi-statically indenting until a predetermined amount of energy had been expended in the elasto-plastic deformation of the material underneath the surface. Spherical shots (indenters) were treated as rigid bodies for this simulation. The energies of these simulations were $\sim 1.4 \times 10^{-6}$ Joules, $\sim 8.8 \times 10^{-5}$ Joules, $\sim 4.1 \times 10^{-4}$ Joules, and ~ 0.001 Joules, which theoretically correspond to velocities of 7.06 m/s, 56.01 m/s, 120.90 m/s, and 188.81 m/s of media. These calculations corresponded to spherical media with a diameter of 350 µm and density of 2500 Kg/m^3. The coefficient of friction between the media and the surface was set as $\mu_f = 0.2$. The surface obtained from white light profilometry of sample 2 in Figure 1b was digitized and transformed into a solid part using the python interface of Abaqus. A cutoff resolution of 16 µm was used for ensuring numerical tractability. Indentation was performed on carefully chosen 'bumpy' and 'smooth' parts of this numerical workpiece, which were characterized in terms of their local Mean curvature (H). Further, indentation was also performed on a smooth flat surface as control. The workpiece material was assigned an elasticity modulus corresponding to Ti6Al4V, e.g., $E = 113.8$ GPa, and an isotropic Johnson–Cook plasticity law with parameters $[A, B, n, m, T_m] = [1098\,\text{MPa}, 1092\,\text{MPa}, 0.93, 1.1, 1941\,\text{K}]$ [45]. After the simulation, changes in the local surface topography and evolution of residual stress fields in the vicinity of the impact were analyzed.

3. Results

3.1. Evolution of Surface Roughness during Bead-Blasting

White light profilometry was used to measure roughness textures before and after bead-blasting of the surface resulting from AM. As-received surfaces aligned at 0° and 30° with respect to the horizontal were studied. These correspond to the top surfaces shown in Figure 1a,b, whose white light characterizations before/after bead-blasting are shown in Figure 3a,b, and Figure 3c,d, respectively. In addition, an electric discharge machined surface obtained from the first sample, i.e., Figure 1a, was also studied, whose white light characterization before/after bead-blasting is shown in Figure 3e,f, respectively. Surface roughness was measured on the overall surface, i.e., no cut-off wavelength was used. However, due to the high roughness in the 30° surface, there were ghost errors present in the profilometry. They were filtered out using a cut-off wavelength of 25 µm.

The surfaces exhibited a decrease in roughness values with respect to all three roughness parameters. These changes are reported in Table 1 using parameters S_a, S_q, and S_z, which correspond to the arithmetic mean height, root mean square height and maximum height, respectively. Percentage reductions in these parameters are $(\Delta S_a, \Delta S_q, \Delta S_z)$ = (57.38%, 55.42%, 29.09%), (52.05%, 49.16%, 5.21%), (76.82%, 66.09%, 68.47%), for 0° as-received, 0° EDM, and 30° as-received surfaces, respectively. The results are shown in Figure 4.

Table 1. Roughness characteristics S_a, S_q, and S_z and their surface residual stresses.

Roughness Parameter	S_a (µm)		S_q (µm)		S_z (µm)		Res. Stress (MPa)	
	Before	After	Before	After	Before	After	Before	After
Sample 1, cf. Figure 1a								
As-received	5.35	2.28	6.46	2.88	36.54	25.91	−345.07	−517.60
EDM	3.90	1.87	4.78	2.43	27.26	25.84	159.75	−517.60
Sample 2, cf. Figure 1b								
As-received	68.08	15.78	58.18	19.73	346.48	109.25	−121.41	−479.26

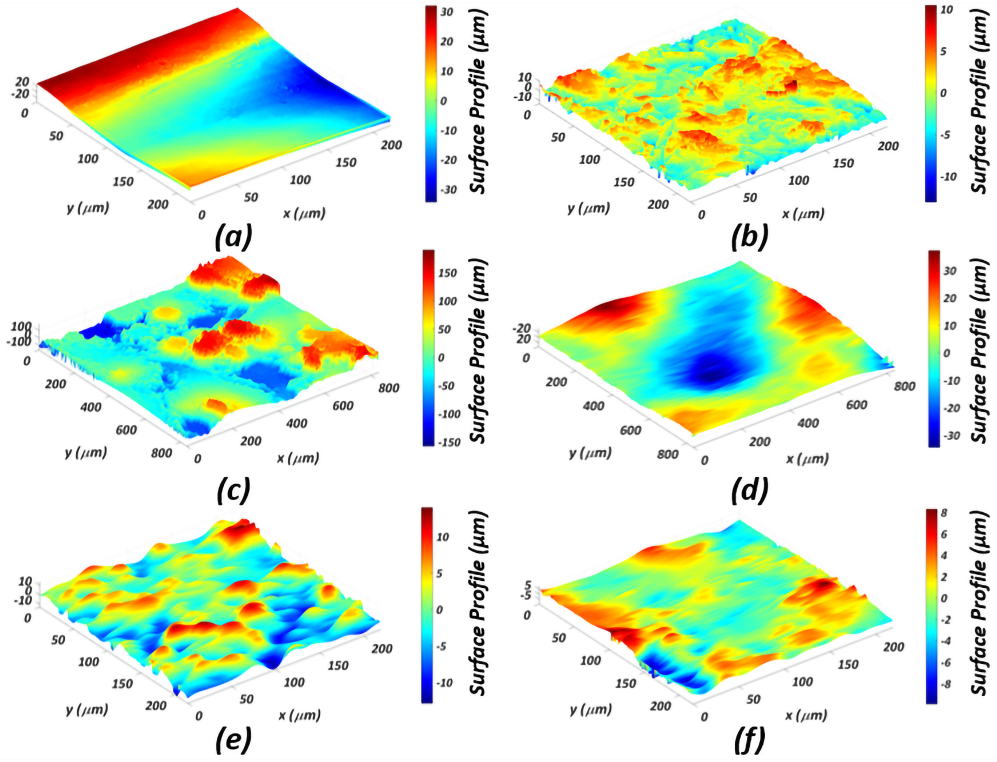

Figure 3. Surface roughness profile of: (**a**) 0° top surface before bead-blasting; (**b**) 0° top surface after bead-blasting; (**c**) 30° top surface before bead-blasting; (**d**) 30° top surface after bead-blasting; (**e**) EDM surface before bead-blasting; (**f**) EDM surface after bead-blasting.

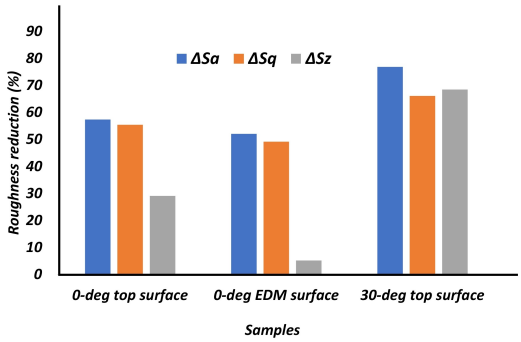

Figure 4. Reduction in surface roughness parameters (%) after bead-blasting of the samples.

The smallest change was seen in the 0° EDM specimen (cf. Figure 3e,f), whereas the largest change was seen in the 30° as-received specimen (cf. Figure 3c,d). Interestingly, these changes were found to be monotonically correlated with the starting roughness values. For instance, the 0° EDM surface which had the smallest average starting roughness showed a decrease in roughness about 52.05% after bead-blasting. In comparison, the 30° top surface that had the highest average starting roughness showed a decrease in roughness of about 76.82%. This suggests that a rougher surface could be expected to exhibit a larger relative decrease in its roughness parameters for the same extent of impact treatment. Nonetheless, the roughest surfaces continued to exhibit high roughness values even after bead-blasting compared to the counterpart surfaces that were smoother to begin with. For instance, the 0° EDM surface showed an average surface roughness of 1.87 µm after bead-blasting. In comparison, the 30° top surface showed an average roughness of 15.78 µm after bead-blasting.

3.2. Evolution of Surface Residual Stresses during Bead-Blasting

The $\sin^2\psi$ method was used to measure residual stress on surfaces in as-received and shot-peened states. This method relies on the characterization of elastic normal strains from diffraction peak shifts and relating them to near-surface bi-axial stress σ_Φ via Equation [46]:

$$\varepsilon_{\Phi\psi}^{hkl} = S_x^{\{hkl\}}(\sigma_{xx} + \sigma_{yy}) + \frac{1}{2}S_y^{\{hkl\}}\sigma_\Phi \sin^2\psi \quad (1)$$

Here, $S_x = -\nu/E$ and $\frac{1}{2}S_y = \frac{1+\nu}{E}$ are functions of material constants, viz. Poisson's ratio $\nu = 0.34$ and Young's modulus $E = 113.8$ GPa [47]. The variable $\varepsilon_{\Phi\psi}^{hkl}$ refers to the normal elastic residual strain that was measured from the shift of peak $\{hkl\} = \{10\bar{1}3\}$ using the equation $\varepsilon_{\Phi\psi}^{\{hkl\}} = \frac{d}{d_0} - 1$. Here, d_0 refers to spacing of $\{hkl\}$ planes in the original wrought state and d refers to spacing of the same plane after AM (as-received/EDM/shot-peened) state. The value of d_o at room temperature ($RT = 25$ °C) was used, i.e., $d_{10\bar{1}3} = 1.329$ Å [48]. This formulation requires measuring elastic normal strains at various ψ values that can be then fit as linear functions of $\sin^2\psi$ using Equation (1), whose slope can then provide the residual stress σ_Φ. Ten measurements were taken per specimen, and these plots are shown in Figure 5.

The measured values of peak shifts for various values of ψ exhibited linear variations with respect to $\sin^2\psi$. The corresponding linear fits exhibited coefficients of determination $R^2 = 0.940$, 0.976, 0.656, 0.958, 0.096, and 0.972, respectively, for plots in Figure 5a–f, respectively. These plots correspond to measurements on 0° as-received, 30° as-received, and 0° EDM surfaces before and after bead-blasting, respectively. The corresponding values of residual stresses are listed in Table 1. Before bead-blasting, all but the EDMed surface exhibited compressive residual stresses. Tensile residual stress are often seen in as-built conditions after EDM, which might explain the behavior seen here [49,50]. Further, residual stress in as-received conditions were more compressive in the 0° as-received surface (∼−345.07 MPa) compared to the 30° as-received surface (∼−121.41 MPa). However, after bead-blasting using equivalent parameters, all surfaces exhibited highly compressive residual stresses. Herein, the maximum compressive stresses were seen in the 0° as-received (∼−517.60 MPa) and EDM surface (∼−517.60 MPa) compared to the 30° surface that exhibited a slightly smaller compressive residual stress (∼−479.26 MPa).

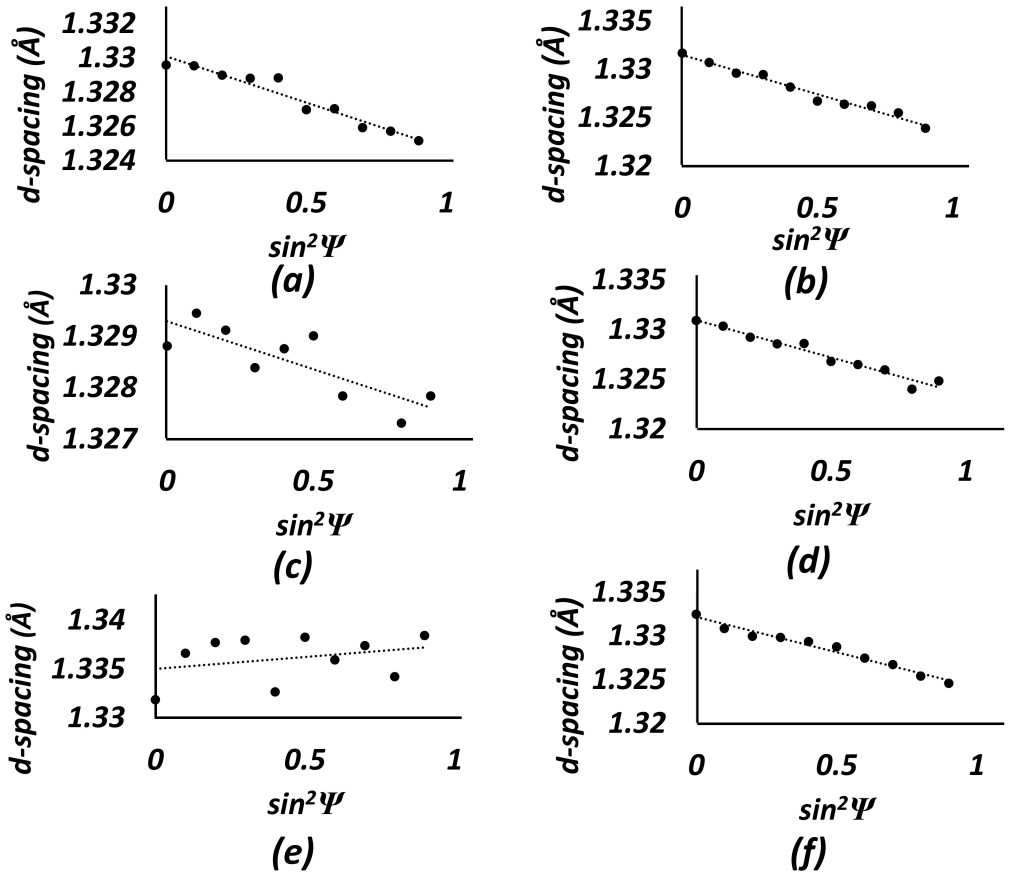

Figure 5. Plot of d-spacing vs. $\sin^2\psi$ of: (**a**) 0° top surface before bead-blasting; (**b**) 0° top surface after bead-blasting; (**c**) 30° top surface before bead-blasting; (**d**) 30° top surface after bead-blasting; (**e**) EDM surface before bead-blasting; (**f**) EDM surface after bead-blasting.

4. Discussion

4.1. Reduction of Surface Roughness during Bead-Blasting

Reducing surface roughness during bead-blasting involves flattening roughness texture peaks due to impact with incident shots by plastic deformation. Analytical treatments of this phenomena [51,52] suggest that the extent of plastic deformation can be modeled as the average coefficient of restitution e of impacts with respect to the plasticity index $\mathcal{P}$ of the shot-surface system. The coefficient of restitution $e = v_2/v_1$ refers to the ratio of the reflecting velocity of the shot v_2 to its incident velocity v_1. A smaller coefficient of restitution indicates greater plastic deformation resulting from the impact of shot media with a surface, which generally indicates a greater texture flattening/smoothing effect. The plasticity index of the shot-surface system is given by $\mathcal{P} = \frac{2E^*}{\pi KY}\sqrt{\frac{S_q}{R}}$, where E^* given by $\frac{1}{E^*} = \frac{1-\nu_1^2}{E_1} + \frac{1-\nu_2^2}{E_2}$ is the Hertz contact effective Young's modulus of the shot-surface system, $K = 1.282 + 1.158\nu_1$ is the yield coefficient, Y is the yield strength of the surface, S_q is the root mean squared roughness, and R is the radius of the curvature of the roughness texture. Parameters ν_1, E_1, and ν_2, E_2 denote the Poisson's ratio and Elastic Modulus of the workpiece and peening media, respectively. A greater plasticity index results from greater surface roughness characterized as S_q, which is enhanced by the simultaneous presence of roughness texture peaks that feature smaller curvature radii R.

It has been shown that the coefficient of restitution e declines monotonically with an increase in the plasticity index $\mathcal{P}$ [52]. This indicates that a greater plasticity index, i.e., a rougher surface, generally results in greater plastic strains during an equivalent bead-blasting treatment, which results in greater flattening of roughness textures. In order to test the validity of this behavior for our specimens, plasticity indices were characterized for the

0° as-received, 0° EDM, and 30° as-received surfaces. Parameter E^* was calculated using the Young's modulus and Poisson's ratio of Ti-6Al-4V, i.e., ($E_1 = 113.8$ GPa, $\nu_1 = 0.34$) and that of shot media, i.e., ($E_1 = 70$ GPa, $\nu_1 = 0.22$). The value of K for Ti-6Al-4V was calculated using $\nu_1 = 0.34$ as $K = 1.67572$. The curvature of roughness features was calculated using the approach delineated in refs. [53,54] as $R = 0.375\sqrt{\frac{\pi}{m_4}}$, where $m_4 = \langle \frac{\partial^2 z}{\partial x^2} \rangle$ is the second derivative of the line profile of roughness texture.

Table 2 lists the average radii of curvature and plasticity indices of surfaces in a pre-shot-peened state. The 30° as-received surface exhibited the greatest plasticity index $\mathcal{P} = 716.22, 715.58$ prior to bead-blasting in the x, y directions, respectively, in comparison with the 0° as-received surface, which exhibited $\mathcal{P} = 251.50, 163.19$, and the 0° EDM surface, which exhibited $\mathcal{P} = 88.64, 87.06$. These plasticity indices suggest that the 30° as-received surface would undergo the greatest amount of plastic deformation under an equivalent bead-blasting treatment compared to the 0° as-received surface and the 0° EDM surface, in that order. In this regard, these surfaces should also exhibit analogous texture flattening/smoothing effects, which is indeed the case as summarized in Section 3. For instance, the 30° as-received surface exhibits the greatest reduction in surface roughness of ($\Delta S_a, \Delta S_q, \Delta S_z$) = (76.82%, 66.09%, 68.47%) compared to (57.38%, 55.42%, 29.09%) for the 0° as-received surface and (52.05%, 49.16%, 5.21%) for the 0° EDM surface, respectively.

Table 2. Average radii of curvature R of roughness texture features and corresponding plasticity indices $\mathcal{P}$ of various surface conditions.

Surface Condition	x Direction		y Direction	
	Radius of Curvature R (μm)	Plasticity Index $\mathcal{P}$	Radius of Curvature R (μm)	Plasticity Index $\mathcal{P}$
0° as-received	0.09	251.50	0.67	163.19
0° EDM	0.18	88.64	0.19	87.06
30° as-received	0.03	716.22	0.03	715.58

4.2. Effect of Local Surface Texture on Mechanics of Bead-Blasting

The analysis in Section 4.1 suggests that the spatially averaged efficacy of bead-blasting is highly correlated to spatially averaged metrics of the as-received surface. To delineate the mechanistic underpinnings of these effects, unit impacts were simulated with numerically reconstructed surface texture features relevant to AM. These impacts were implemented with energy control, in which circular beads with a diameter of 350 μm were indented into the surface until a specified amount of energy was expended elasto-plastically. These beads were implemented as rigid bodies to ensure that the elasto-plastic energy expenditure was contributing directly to surface finishing. Two surfaces were used to perform this analysis, the as-received 30-degree top surface shown in Figure 3c and a perfectly flat surface that served as control. Moreover, two different zones from the 30-degree top surface were used. These three incident surfaces were characterized with respect to their mean local surface curvatures H. This parameter is calculated using Equation [55,56]:

$$H = \frac{EN + GL - 2FM}{2(EG - F^2)} \tag{2}$$

Here, E, F, G, and L, M, N are the first and second fundamental coefficients of a surface, respectively. If a surface is parameterized as $\boldsymbol{r}(u,v) = (x(u,v), y(u,v), z(u,v))$, and $\boldsymbol{r}_u = \frac{\partial \boldsymbol{r}}{\partial u}$, $\boldsymbol{r}_v = \frac{\partial \boldsymbol{r}}{\partial v}$, then $E = \boldsymbol{r}_u \cdot \boldsymbol{r}_u$, $F = \boldsymbol{r}_u \cdot \boldsymbol{r}_v$, $G = \boldsymbol{r}_v \cdot \boldsymbol{r}_v$. Further, $L = \boldsymbol{r}_{uu} \cdot \boldsymbol{n}$, $M = \boldsymbol{r}_{uv} \cdot \boldsymbol{n}$ and $N = \boldsymbol{r}_{vv} \cdot \boldsymbol{n}$, where $\boldsymbol{n}(u,v)$ is a vector, normal to the surface $\boldsymbol{r}(u,v)$ at location $(x(u,v), y(u,v), z(u,v))$. It is realized that the mean surface curvature values can depend on the area of the zone selected for their characterization. This complication was resolved by characterizing the parameter H with respect to increasingly larger areas around the points of indentation. From this variation, the smallest converging values of the mean

curvature were selected to characterize the incident surface zones. Figure 6a shows the original unfiltered 30-deg top-surface profile. Complications that may arise from stochastic noise originating from the profilometer were eliminated by applying Gaussian low-pass filters to the surface profiles in the frequency space. This low-pass filter selectively subdued very high frequencies in the surface profile (see Figure 6b) while preserving roughness texture features relevant to the larger length scales relevant to our numerical indentation experiments. Figure 6c shows the generation of this 30 deg top-surface in the FEA model. The numerical indentation experiments were performed on locations 1 and 2, which are demarcated in Figure 6a–c. These locations were characterized with respect to their mean surface curvature as $H = 5.6 \times 10^{-3}$ μm^{-1}, and $H = -6.6 \times 10^{-3}$ μm^{-1}, respectively. The mean curvature fields of these convex and concave zones are shown in Figure 6d,e, respectively, which correspond to an area of 80 pixels × 80 pixels or ~4265 μm^2. Finally, the mean surface curvature of the perfectly flat control surface was $H = 0$ μm^{-1}.

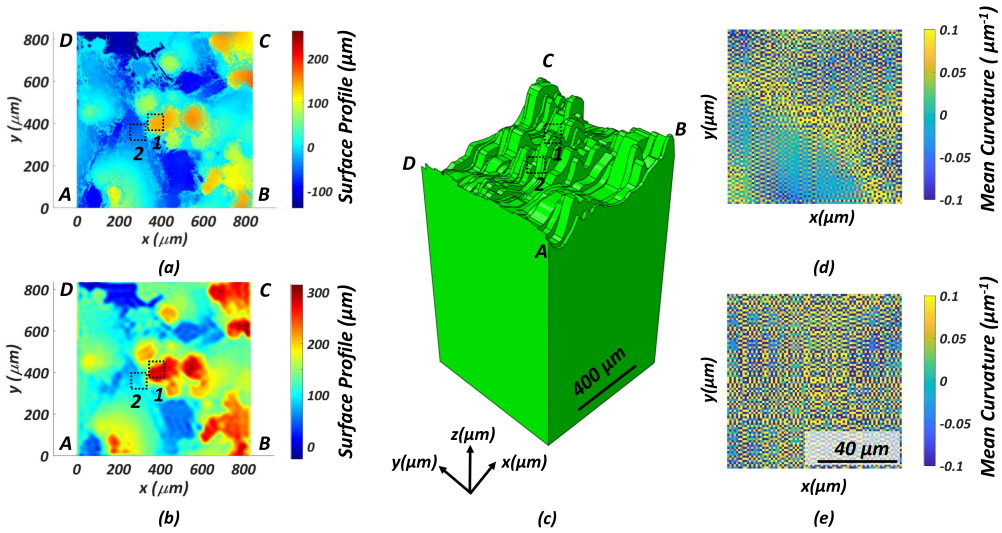

Figure 6. (**a**) Non-filtered 30 deg top-surface profile; (**b**) Filtered 30 deg top-surface profile. A–D points are the four corners of the profile and blue and orange dashed box 1,2 indicate the convex and concave zones, respectively; (**c**) 30 deg top-surface generated in the FEA model showing the relative location of points 1 and 2; (**d**) Mean curvature field for the area surrounding the convex feature; (**e**) Mean curvature field for the area surrounding the concave feature.

The response of these surfaces to the incident beads were characterized as their energy absorption characteristics. The elasto-plastic strain energy absorbed by the surface is calculated in ABAQUS and available using the variable ALLSE. This energy is given by the formulation:

$$U = \sum_{i=1}^{N} \int_{\underset{\sim}{0}}^{\underset{\sim}{\epsilon_i}} V_i \underset{\sim}{\sigma_i} d\underset{\sim}{\epsilon_i} \quad (3)$$

Here, N is the total number of elements, V_i is the volume of an element i, $\underset{\sim}{\sigma_i}$ is the Cauchy stress tensor, and $\underset{\sim}{\epsilon_i}$ is the strain tensor of element i. Implementation of this concept is shown in Figure 7a–d, corresponding to preset energy values of $E = 1.4 \times 10^{-6}$ J, 8.8×10^{-5} J, 4.1×10^{-4} J, and 1×10^{-3} J, respectively. These plots exhibit unique characteristics that result from the nature of the engagement of the incident shot with the substrate. The maximum indentation depths and rate of energy expenditure were extracted from these curves and are summarized in Figure 8a,b, respectively.

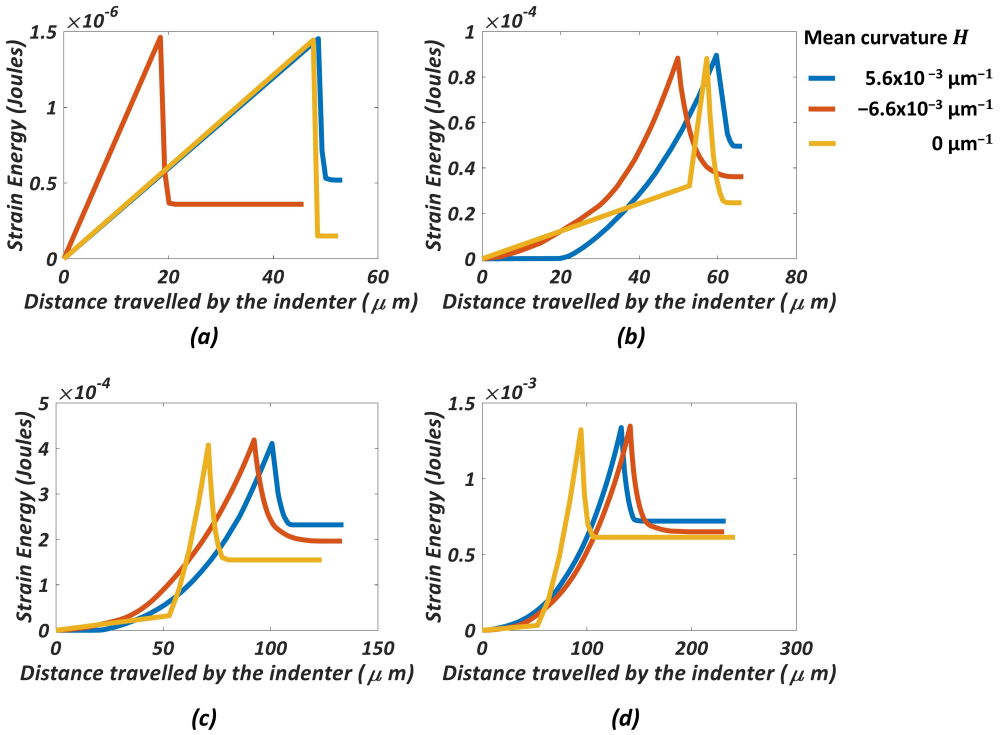

Figure 7. Elasto-plasticenergy exchange characteristics during indentation and retraction. Preset energies were: (**a**) 1.4×10^{-6} J; (**b**) 8.8×10^{-5} J; (**c**) 4.1×10^{-4} J; (**d**) 1×10^{-3} J.

The correlations between spatially averaged metrics of surface roughness and efficacy of surface smoothing described in Section 4.1 are also seen here. At every energy level studied, the maximum z_{max} as well as the retained indentation depths left after the retraction of indenter z_{ret} exhibited high correlations with respect to the incident energy E of the indenting bead. These could be quantified as linear relations, e.g., $z = m_{slope}E + c$, with goodness of fits $R^2 > 0.92$ in all cases. Nonetheless, these controlled numerical simulations enabled the delineation of the evolution of surface roughness textures during bead-blasting as a function of their local surface curvature. For instance, at lower energies, the convex and concave roughness textures exhibited considerably different maximum z_{max} and retained z_{ret} depths. This discrepancy was subdued at higher incident energy levels. These evolutions are characterized as ratios between parameters z_{max} and z_{ret} for various energies, e.g., $\frac{z_{max:H=5.6\times10^{-3}}}{z_{max:H=-6.6\times10^{-3}}} \sim 2.64,\ 1.20,\ 1.10\ 0.94$, and $\frac{z_{ret:H=5.6\times10^{-3}}}{z_{ret:H=-6.6\times10^{-3}}} \sim 2.90,\ 1.54,\ 1.58\ 1.32$, for $E_{incident} = 1.4 \times 10^{-6}$ J, 8.8×10^{-5} J, 4.1×10^{-4} J, and 1×10^{-3} J, respectively. A microstructural manifestation of this effect was also witnessed during sand-blasting of oxygen-free high-conductivity copper [57]. The crystallographic textures of microstructures in sand-blasted volumes exhibited a similar saturation at high levels of effective strain, which can be likened to a higher level of incident energy.

The results described in the previous paragraph suggest that the propensity of a surface to dissipate the energy of incoming beads during blasting depends on local surface curvatures of their roughness textures. This is quantified as the derivative dE/dz, where E is the elasto-plastic energy of the numerical substrate shown in Figure 6c and z is the current depth of indentation. Figure 8b summarizes this derivative for the convex and concave textures studied in this research using blue and red curves, respectively. This figure also summarizes energy absorption characteristics of the perfectly flat surface, shown as the yellow curve.

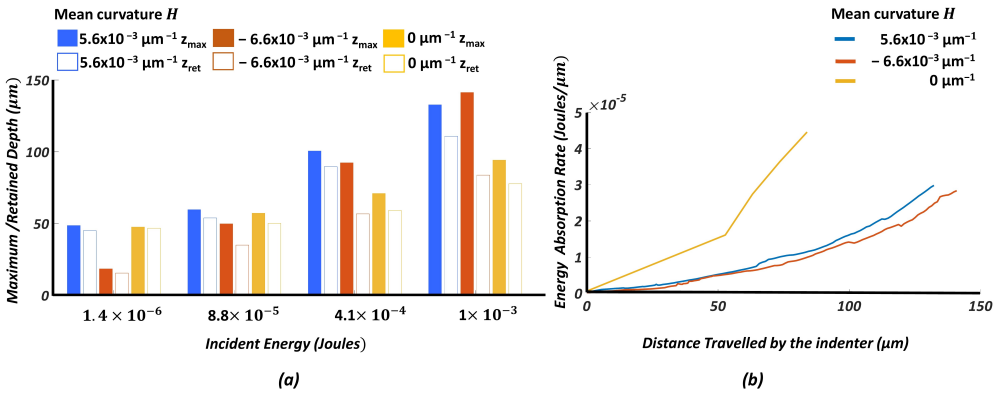

Figure 8. (**a**) Maximum depthobserved in energy-controlled numerical indentation experiment and (**b**) rate of energy absorption.

These results clearly indicate that the mechanics of bead-blasting of rough surfaces can be considerably different than smooth surfaces. In fact, this is true at both low and high indentation depths wherein the energy absorption rates were quantified as $\frac{dE}{dz} = 2.82 \times 10^{-6}$ Joules/µm, 2.41×10^{-6} Joules/µm, 6.09×10^{-7} Joules/µm, and $\frac{dE}{dz} = 1.48 \times 10^{-5}$ Joules/µm, 1.38×10^{-5} Joules/µm, 2.67×10^{-5} Joules/µm, for surfaces with $H = 5.6 \times 10^{-3}$, -6.6×10^{-3}, 0 µm^{-1}, respectively. Further, despite converging behaviors of the two roughness texture features with respect to an achievable depth of indentation at progressively higher incident energies, their energy dissipation characteristics $\frac{dE}{dz}$ exhibit progressively larger differences with respect to each other (see Figure 8b). The reason behind this discrepancy lies in the disparity between the evolution trajectories of roughness texture features, which are likely governed by their local surface curvature in their as-received state, and hardening characteristics.

4.3. Effect of Local Surface Texture on Residual Stresses Resulting from Bead-Blasting

The discrepancies in the mechanical response of surface texture features during bead-blasting (see discussion in Section 4.2) affect the associated residual stress fields. To delineate these effects, σ_{yy} residual stress fields resulting from numerically simulated indentation experiments were analyzed. These are shown in Figure 9 for the largest incident energy level—$E4 = 1 \times 10^{-3}$ Joules—studied in this research. For easy comparison of these stress fields, the color bar was limited between -1.013×10^2 and 1.016×10^3 MPa. This range comprised about 90% of the total material volume in all cases. Nonetheless, the real (minima, maxima) values are specified in Figure 9 and were $(-3.90 \times 10^4$ MPa, 3.15×10^4 MPa), $(-4.56 \times 10^4, 5.74 \times 10^4$ MPa), $(-1.27 \times 10^4$ MPa, 1.38×10^4 MPa) for Figure 9a–c, respectively.

These profiles show that residual stresses extend to depths of approximately (108.80 µm, 67.31 µm, 131.50 µm), (142.60 µm, 139.88 µm, 139.90 µm), (305.40 µm, 176.30 µm, 193.10 µm), and (389.90 µm, 299.20 µm, 397.80 µm) for energy levels 1.4×10^{-6} J, 8.8×10^{-5} J, 4.1×10^{-4} J, and 1×10^{-3} J for surfaces featuring $H = 5.6 \times 10^{-3}$ µm^{-1}, -6.6×10^{-3} µm^{-1}, 0 µm^{-1}, respectively. These distances are demarcated in Figure 10 and correspond to depths at which residual stresses decay to within ±10 MPa and stop fluctuating. Further, the residual stresses on the concave surface zone, e.g., $H = -6.6 \times 10^{-3}$ µm^{-1} (c.f. zone 2 in Figure 6), exhibited more compressive characteristics compared to flat $H = 0$ µm or convex surface zones $H = 5.6 \times 10^{-3}$ µm (c.f. zone 1 in Figure 6). Indentation-based models of shot-peening implemented using FEA [58–61] report similar depths for flat surfaces, e.g., ∼400 µm, from the surface.

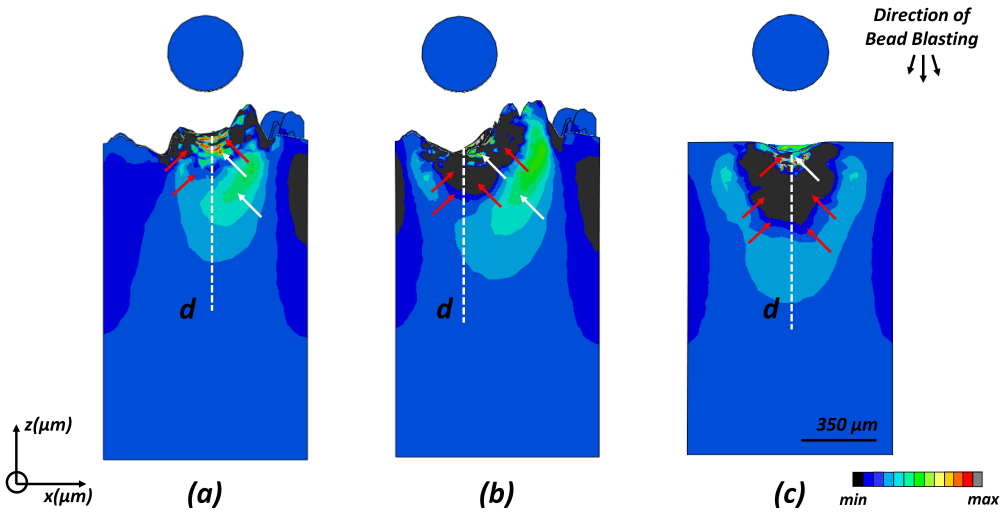

Figure 9. Simulated residual stress profile left after indentation: (**a**) Zone with mean curvature 5.6×10^{-3} μm^{-1}. The (maxima, minima) values of stress field are $(3.15 \times 10^4$ MPa, -3.90×10^4 MPa$)$. (**b**) Zone with mean curvature -6.6×10^{-3} μm^{-1}. The (maxima, minima) values of stress field are $(5.74 \times 10^4$ MPa, -4.56×10^4 MPa$)$. (**c**) Zone with mean curvature 0, i.e., ideal flat surface. The (maxima, minima) values of stress field are $(1.38 \times 10^4$ MPa, -1.27×10^4 MPa$)$. The residual stress field is plotted within a limit of Maximum, Minimum values of -1.013×10^2 to 1.016×10^3 MPa. Elements having stress above this range are colored grey and below this range are colored black. The white and red arrows indicate positive and negative residual stress values, respectively.

It is clear from these plots that the nature of surface texture critically governs not just the maxima and minima of residual stress fields but also their spatial profiles. This is most obvious when comparing Figure 9b (e.g., $H = -6.6 \times 10^{-3}$ μm^{-1}) with Figure 9c (e.g., $H = 0$ μm^{-1}). In the former, a large fraction of spatial volume that features high values of compressive stresses is found to the right side of the central axis, whereas in the latter, a largely symmetric arrangement is shown. To quantify this effect, stress vs. depth profiles were extracted for the three cases studied here. This was conducted for all four incident energy levels, and the results are shown in Figure 10.

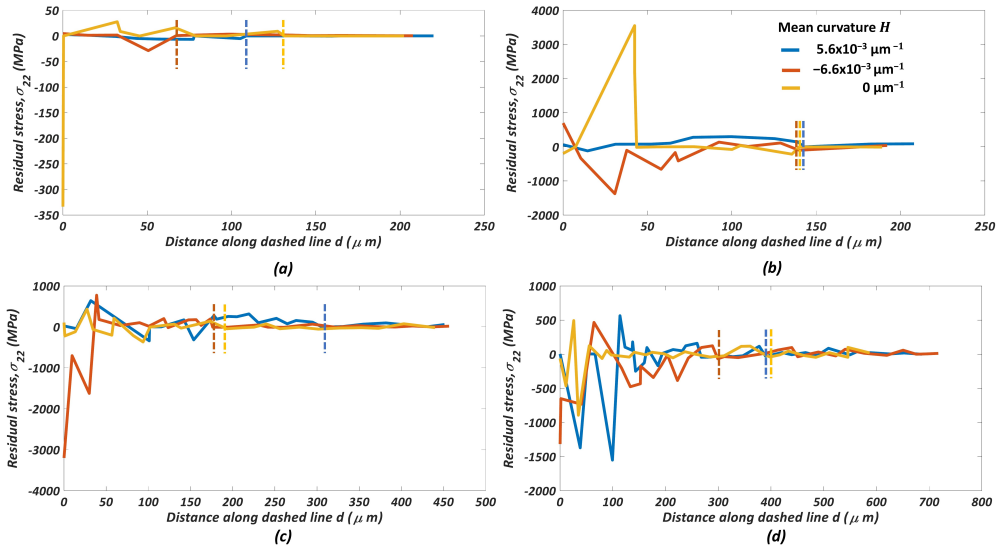

Figure 10. Residual stress depth profile: (**a**) energy level E1 $\sim 1.4 \times 10^{-6}$ Joules; (**b**) energy level E2 $\sim 8.8 \times 10^{-5}$ Joules; (**c**) energy level E3 $\sim 4.1 \times 10^{-4}$ Joules; (**d**) energy level E4 $\sim 1 \times 10^{-3}$ Joules. The dashed lines show the distance from the surface after which the stress profile becomes stable.

We note that there are different sources of inhomogeneity in AM components. In previous studies that focused on indentation of Inconel 718 [18,62], the authors explored the combined effect of surface roughness and void inhomogeneities on the mechanics of indentation. Using numerical simulations, the authors have also realized that the nature of the inhomogeneities characterized by their shape, size, aspect ratio [63], and location within the part geometry [64] complicate the mechanical response of components. However, these variables are not tested in the context of bead-blasting in this study. This choice has enabled the authors to focus on just surface roughness characteristics. Insights from this study are still relevant to some real fabrication routines, e.g., those in which the component has already undergone hot isostatic pressing (HIP) to eradicate void-like defects prior to bead-blasting. This preserves the beneficial compressive stresses that often result from the mechanical action of bead-blasting, which would be eradicated if HIP was performed afterwards due to thermal perturbation there.

5. Conclusions

In this study, the effects of the as-received surface texture on the bead-blasting process were characterized. Particular focus was given to the evolution of the surface texture and residual stresses. The following conclusions can be drawn:

1. The surface smoothing effect resulting from bead-blasting was found to be correlated to as-received roughness. Specifically, surfaces with greater roughness exhibited a greater fractional reduction in roughness. The preliminary analysis showed that this correlation was rooted in the plasticity index, $\mathcal{P}$, of the as-received surfaces.
2. The residual stress distribution resulting from a single bead impact was found to be highly sensitive to the texture of the affected surface. Specifically, it was determined that the local mean curvature affects the energy absorption and release characteristics of a surface. A bead striking an asperity (e.g., positive local mean curvature) resulted in fluctuations between compressive and tensile residual stress at and just below the affected surface—a condition that is detrimental to the objective of bead-blasting. Much smaller distributions of tensile stresses were observed for a bead striking a surface with a negative local mean curvature. They were still smaller for a bead striking a nominally flat surface.

Bead blasting cannot be employed indefinitely to a surface with the objective of increasingly smoothing it. Eventually, the affected metal strain hardens and loses ductility to the extent that additional impact results in no additional plastic deformation but instead induces cracking and fracture [65]. This phenomenon is referred to as over-coverage. The results from this study indicate the possibility that the rough surfaces produced by EBPBF may be prone to the detrimental effects of over-coverage due to the initial development of tensile residual stresses at the asperities. Additional research is needed to prove whether this is true for repeated bead contact. Additionally, while bead-blasting was shown to improve the roughness of a 30° inclined surface from $S_a = 68$ µm to $S_a = 16$ µm, the reduction is still insufficient to satisfy most applications where fatigue is of concern. This suggests that a combination of secondary machining and bead-blasting may be needed to transform a printed, non-functional surface into one that is optimized for fatigue resistance.

Author Contributions: M.R. established the experimental setup for collecting data, collected data, performed analysis, ran computational code to collect, analyzed computational data, and wrote the preliminary draft of the manuscript. S.B. wrote computational codes, performed the analysis, edited the manuscript, and wrote some sections. E.C.D.M. performed the analysis, edited the manuscript, and wrote some sections. G.M. provided the additive-manufactured specimens used in this study. All authors have read and agreed to the published version of the manuscript.

Funding: S.B. would like to acknowledge partial support from the NSF grant 1825686. Any opinions, findings, conclusions, or recommendations expressed in this material are those of the authors and do not necessarily reflect the views of the National Science Foundation.

Institutional Review Board Statement: Not applicable.

Informed Consent Statement: Not applicable.

Data Availability Statement: The data used for research described in this manuscript are available upon request from the corresponding author Saurabh Basu (email: sxb514@psu.edu).

Conflicts of Interest: The authors declare no conflict of interest.

References

1. Cabanettes, F.; Joubert, A.; Chardon, G.; Dumas, V.; Rech, J.; Grosjean, C.; Dimkovski, Z. Topography of as built surfaces generated in metal additive manufacturing: A multi scale analysis from form to roughness. *Precis. Eng.* **2018**, *52*, 249–265. [CrossRef]
2. Snyder, J.C.; Stimpson, C.K.; Thole, K.A.; Mongillo, D.J. Build direction effects on microchannel tolerance and surface roughness. *J. Mech. Des.* **2015**, *137*, 111411. [CrossRef]
3. Aguado-Montero, S.; Navarro, C.; Vázquez, J.; Lasagni, F.; Slawik, S.; Domínguez, J. Fatigue behaviour of PBF additive manufactured TI6AL4V alloy after shot and laser peening. *Int. J. Fatigue* **2022**, *154*, 106536. [CrossRef]
4. Bagehorn, S.; Wehr, J.; Maier, H. Application of mechanical surface finishing processes for roughness reduction and fatigue improvement of additively manufactured Ti-6Al-4V parts. *Int. J. Fatigue* **2017**, *102*, 135–142. [CrossRef]
5. Wu, J.; Liu, H.; Wei, P.; Lin, Q.; Zhou, S. Effect of shot peening coverage on residual stress and surface roughness of 18CrNiMo7-6 steel. *Int. J. Mech. Sci.* **2020**, *183*, 105785. [CrossRef]
6. Gariépy, A.; Miao, H.; Lévesque, M. Simulation of the shot peening process with variable shot diameters and impacting velocities. *Adv. Eng. Softw.* **2017**, *114*, 121–133. [CrossRef]
7. Maliwemu, E.U.K.; Malau, V.; Iswanto, P.T. Effect of shot peening in different shot distance and shot angle on surface morphology, surface roughness and surface hardness of 316L biomaterial. *IOP Conf. Ser. Mater. Sci. Eng.* **2018**, *299*, 012051. [CrossRef]
8. Sasikumar, K.; Dineshkumar, K.; Deeban, K.; Sambathkumar, M.; Saravanan, N. Effect of shot peening on surface properties of Al7075 hybrid aluminum metal matrix composites. *Mater. Today Proc.* **2020**, *33*, 2792–2794. [CrossRef]
9. Maleki, E.; Unal, O. Shot peening process effects on metallurgical and mechanical properties of 316 L steel via: Experimental and neural network modeling. *Met. Mater. Int.* **2021**, *27*, 262–276. [CrossRef]
10. Walczak, M.; Szala, M. Effect of shot peening on the surface properties, corrosion and wear performance of 17-4PH steel produced by DMLS additive manufacturing. *Arch. Civ. Mech. Eng.* **2021**, *21*, 157. [CrossRef]
11. Zhao, X.; Zhou, H.; Liu, Y. Effect of shot peening on the fatigue properties of nickel-based superalloy GH4169 at high temperature. *Results Phys.* **2018**, *11*, 452–460. [CrossRef]
12. Maleki, E.; Bagherifard, S.; Unal, O.; Bandini, M.; Farrahi, G.H.; Guagliano, M. Introducing gradient severe shot peening as a novel mechanical surface treatment. *Sci. Rep.* **2021**, *11*, 22035. [CrossRef] [PubMed]
13. Shukla, P.P.; Swanson, P.T.; Page, C.J. Laser shock peening and mechanical shot peening processes applicable for the surface treatment of technical grade ceramics: A review. *Proc. Inst. Mech. Eng. Part B J. Eng. Manuf.* **2014**, *228*, 639–652. [CrossRef]
14. Pfeiffer, W.; Frey, T. Advances in shot peening of silicon nitride ceramics. In Proceedings of the International Conference and Exhibition on Shot Peening, ICSP9, Paris, France, 6–9 September 2005; pp. 326–331.
15. Frey, T.; Pfeiffer, W. Shot peening of ceramics: Damage or benefit. *Ceram Forum Int.* **2006**, *79*, 187–190.
16. Hassani-Gangaraj, S.; Moridi, A.; Guagliano, M.; Ghidini, A.; Boniardi, M. The effect of nitriding, severe shot peening and their combination on the fatigue behavior and micro-structure of a low-alloy steel. *Int. J. Fatigue* **2014**, *62*, 67–76. [CrossRef]
17. Sherafatnia, K.; Farrahi, G.H.; Mahmoudi, A.H. Effect of initial surface treatment on shot peening residual stress field: Analytical approach with experimental verification. *Int. J. Mech. Sci.* **2018**, *137*, 171–181. [CrossRef]
18. Rifat, M.; DeMeter, E.C.; Basu, S. Microstructure evolution during indentation of Inconel-718 created by additive manufacturing. *Mater. Sci. Eng. A* **2020**, *781*, 139204. [CrossRef]
19. Zhao, C.; Shi, C.; Wang, Q.; Zhao, C.; Gao, Y.; Yang, Q. Residual stress field of high-strength steel after shot peening by numerical simulation. *J. Mater. Eng. Perform.* **2020**, *29*, 358–364. [CrossRef]
20. Basu, S.; Wang, Z.; Saldana, C. Deformation heterogeneity and texture in surface severe plastic deformation of copper. *Proc. R. Soc. A Math. Phys. Eng. Sci.* **2016**, *472*, 20150486. [CrossRef]
21. Basu, S.; Wang, Z.; Saldana, C. Crystallographic textures produced during sand blasting. *Int. Manuf. Sci. Eng. Conf.* **2015**, *56833*, V002T01A006.
22. Hatamleh, O.; DeWald, A. An investigation of the peening effects on the residual stresses in friction stir welded 2195 and 7075 aluminum alloy joints. *J. Mater. Process. Technol.* **2009**, *209*, 4822–4829. [CrossRef]
23. Sidhom, N.; Laamouri, A.; Fathallah, R.; Braham, C.; Lieurade, H. Fatigue strength improvement of 5083 H11 Al-alloy T-welded joints by shot peening: Experimental characterization and predictive approach. *Int. J. Fatigue* **2005**, *27*, 729–745. [CrossRef]
24. Arifvianto, B.; Mahardika, M.; Dewo, P.; Iswanto, P.; Salim, U.A. Effect of surface mechanical attrition treatment (SMAT) on microhardness, surface roughness and wettability of AISI 316L. *Mater. Chem. Phys.* **2011**, *125*, 418–426. [CrossRef]
25. Arifvianto, B.; Mahardika, M. Effects of surface mechanical attrition treatment (SMAT) on a rough surface of AISI 316L stainless steel. *Appl. Surf. Sci.* **2012**, *258*, 4538–4543. [CrossRef]
26. Xu, Z.; Dunleavey, J.; Antar, M.; Hood, R.; Soo, S.; Kucukturk, G.; Hyde, C.; Clare, A. The influence of shot peening on the fatigue response of Ti-6Al-4V surfaces subject to different machining processes. *Int. J. Fatigue* **2018**, *111*, 196–207. [CrossRef]

27. Shivpuri, R.; Cheng, X.; Mao, Y. Elasto-plastic pseudo-dynamic numerical model for the design of shot peening process parameters. *Mater. Des.* **2009**, *30*, 3112–3120. [CrossRef]
28. Maleki, E.; Bagherifard, S.; Bandini, M.; Guagliano, M. Surface post-treatments for metal additive manufacturing: Progress, challenges, and opportunities. *Addit. Manuf.* **2021**, *37*, 101619. [CrossRef]
29. Kahlin, M.; Ansell, H.; Basu, D.; Kerwin, A.; Newton, L.; Smith, B.; Moverare, J. Improved fatigue strength of additively manufactured Ti6Al4V by surface post processing. *Int. J. Fatigue* **2020**, *134*, 105497. [CrossRef]
30. Manogharan, G.; Wysk, R.A.; Harrysson, O.L. Additive manufacturing–integrated hybrid manufacturing and subtractive processes: Economic model and analysis. *Int. J. Comput. Integr. Manuf.* **2016**, *29*, 473–488. [CrossRef]
31. Zhang, L.C.; Liu, Y.; Li, S.; Hao, Y. Additive manufacturing of titanium alloys by electron beam melting: A review. *Adv. Eng. Mater.* **2018**, *20*, 1700842. [CrossRef]
32. Fousová, M.; Vojtěch, D.; Doubrava, K.; Daniel, M.; Lin, C.F. Influence of inherent surface and internal defects on mechanical properties of additively manufactured Ti6Al4V alloy: Comparison between selective laser melting and electron beam melting. *Materials* **2018**, *11*, 537. [CrossRef] [PubMed]
33. Nicoletto, G.; Konečná, R.; Frkáň, M.; Riva, E. Surface roughness and directional fatigue behavior of as-built EBM and DMLS Ti6Al4V. *Int. J. Fatigue* **2018**, *116*, 140–148. [CrossRef]
34. Maizza, G.; Caporale, A.; Polley, C.; Seitz, H. Micro-macro relationship between microstructure, porosity, mechanical properties, and build mode parameters of a selective-electron-beam-melted Ti-6Al-4V alloy. *Metals* **2019**, *9*, 786. [CrossRef]
35. Covarrubias, E.E.; Eshraghi, M. Effect of build angle on surface properties of nickel superalloys processed by selective laser melting. *JOM* **2018**, *70*, 336–342. [CrossRef]
36. Strano, G.; Hao, L.; Everson, R.M.; Evans, K.E. Surface roughness analysis, modelling and prediction in selective laser melting. *J. Mater. Process. Technol.* **2013**, *213*, 589–597. [CrossRef]
37. Ni, C.; Shi, Y.; Liu, J. Effects of inclination angle on surface roughness and corrosion properties of selective laser melted 316L stainless steel. *Mater. Res. Express* **2018**, *6*, 036505. [CrossRef]
38. Shanbhag, G.; Wheat, E.; Moylan, S.; Vlasea, M. Effect of specimen geometry and orientation on tensile properties of Ti-6Al-4V manufactured by electron beam powder bed fusion. *Addit. Manuf.* **2021**, *48*, 102366. [CrossRef]
39. Soyama, H.; Macodiyo, D. Fatigue strength improvement of gears using cavitation shotless peening. *Tribol. Lett.* **2005**, *18*, 181–184. [CrossRef]
40. Wang, T.; Yu, J.; Dong, B. Surface nanocrystallization induced by shot peening and its effect on corrosion resistance of 1Cr18Ni9Ti stainless steel. *Surf. Coat. Technol.* **2006**, *200*, 4777–4781. [CrossRef]
41. Azar, V.; Hashemi, B.; Yazdi, M.R. The effect of shot peening on fatigue and corrosion behavior of 316L stainless steel in Ringer's solution. *Surf. Coat. Technol.* **2010**, *204*, 3546–3551. [CrossRef]
42. Ren, X.; Li, H.; Guo, H.; Shen, F.; Qin, C.; Zhao, E.; Fang, X. A comparative study on mechanical properties of Ti–6Al–4V alloy processed by additive manufacturing vs. traditional processing. *Mater. Sci. Eng. A* **2021**, *817*, 141384. [CrossRef]
43. Ahn, J.; He, E.; Chen, L.; Wimpory, R.; Dear, J.; Davies, C. Prediction and measurement of residual stresses and distortions in fibre laser welded Ti-6Al-4V considering phase transformation. *Mater. Des.* **2017**, *115*, 441–457. [CrossRef]
44. Noyan, I.C.; Cohen, J.B. *Residual Stress: Measurement by Diffraction and Interpretation*; Springer: New York, NY, USA, 2013.
45. Gregory, K. *Failure Modeling of Titanium Ti6Al-4V and Aluminum 2024-T3 with the Johnson-Cook Material Model*; Department of Transportation Federal Aviation Administration: Livermore, CA, USA, 2003.
46. He, B.B. *Two-Dimensional X-ray Diffraction*; Wiley Online Library: Hoboken, NJ, USA, 2009; Volume 2.
47. Alamos, F.J.; Philo, M.; Go, D.B.; Schmid, S.R. Asperity contact under creep conditions. *Tribol. Int.* **2021**, *160*, 107039. [CrossRef]
48. Montanari, R.; Costanza, G.; Tata, M.; Testani, C. Lattice expansion of Ti–6Al–4V by nitrogen and oxygen absorption. *Mater. Charact.* **2008**, *59*, 334–337. [CrossRef]
49. Holmberg, J.; Wretland, A.; Berglund, J.; Beno, T. Surface integrity after post processing of EDM processed Inconel 718 shaft. *Int. J. Adv. Manuf. Technol.* **2018**, *95*, 2325–2337. [CrossRef]
50. Schneider, S.; Vorspohl, J.; Frerichs, F.; Klink, A.; Meinke, M.; Schröder, W.; Lübben, T. Investigation on residual stress induced by multiple EDM discharges. *Procedia CIRP* **2021**, *102*, 482–487. [CrossRef]
51. Greenwood, J.A.; Williamson, J.P. Contact of nominally flat surfaces. *Proc. R. Soc. Lond. Ser. A Math. Phys. Sci.* **1966**, *295*, 300–319.
52. Chang, W.R.; Ling, F.F. Normal impact model of rough surfaces. *J. Tribol.* **1992**, *114*, 439–447. [CrossRef]
53. Kalin, M.; Pogačnik, A.; Etsion, I.; Raeymaekers, B. Comparing surface topography parameters of rough surfaces obtained with spectral moments and deterministic methods. *Tribol. Int.* **2016**, *93*, 137–141. [CrossRef]
54. McCool, J.I. Relating profile instrument measurements to the functional performance of rough surfaces. *J. Tribol.* **1987**, *109*, 264–270. [CrossRef]
55. Kenmotsu, K. *Surfaces with Constant Mean Curvature*; American Mathematical Soc.: Providence, RI, USA 2003; Number 221.
56. Choi, G.; Dudte, L.H.; Mahadevan, L. Programming shape using kirigami tessellations. *Nat. Mater.* **2019**, *18*, 999–1004. [CrossRef] [PubMed]
57. Wang, Z.; Rifat, M.; Saldana, C.; Basu, S. Quantifying the spread in crystallographic textures due to transients in strain path in shot-peening. *Materialia* **2018**, *2*, 231–249. [CrossRef]

58. Song, X.; Liu, W.; Belnoue, J.; Dong, J.; Wu, G.; Ding, W.; Kimber, S.; Buslaps, T.; Lunt, A.; Korsunsky, A. An eigenstrain-based finite element model and the evolution of shot peening residual stresses during fatigue of GW103 magnesium alloy. *Int. J. Fatigue* **2012**, *42*, 284–295. [CrossRef]
59. Klemenz, M.; Schulze, V.; Rohr, I.; Löhe, D. Application of the FEM for the prediction of the surface layer characteristics after shot peening. *J. Mater. Process. Technol.* **2009**, *209*, 4093–4102. [CrossRef]
60. Astaraee, A.H.; Bagherifard, S.; Bradanini, A.; Duó, P.; Henze, S.; Taylor, B.; Guagliano, M. Application of shot peening to case-hardened steel gears: The effect of gradient material properties and component geometry. *Surf. Coat. Technol.* **2020**, *398*, 126084. [CrossRef]
61. Majzoobi, G.; Azizi, R.; Nia, A.A. A three-dimensional simulation of shot peening process using multiple shot impacts. *J. Mater. Process. Technol.* **2005**, *164*, 1226–1234. [CrossRef]
62. Rifat, M.; Basu, S. Deformation Behavior of Grains Near Defects in Direct Metal Laser Sintered Inconel 718 During Indentation. *Int. Manuf. Sci. Eng. Conf.* **2020**, *84256*, V001T01A042.
63. Khanolkar, P.M.; McComb, C.C.; Basu, S. Predicting elastic strain fields in defective microstructures using image colorization algorithms. *Comput. Mater. Sci.* **2021**, *186*, 110068. [CrossRef]
64. Jiang, P.; Edward, C.; Basu, S. The influence of defects on the elastic response of lattice structures resulting from additive manufacturing. *Comput. Mater. Sci.* **2021**, *199*, 110716. [CrossRef]
65. Ganesh, P.; Sundar, R.; Kumar, H.; Kaul, R.; Ranganathan, K.; Hedaoo, P.; Tiwari, P.; Kukreja, L.; Oak, S.; Dasari, S.; et al. Studies on laser peening of spring steel for automotive applications. *Opt. Lasers Eng.* **2012**, *50*, 678–686. [CrossRef]